Chemistry
Europe
European Chemical
Societies Publishing

Membrane-electrode assembly design parameters for optimal CO_2 reduction

Oyinkansola Romiluyi[1,2,3] | **Nemanja Danilovic**[3] | **Alexis T. Bell**[1,2] |
Adam Z. Weber[2,3]

[1]Department of Chemical and Biomolecular Engineering, University of California Berkeley, Berkeley, California, USA

[2]Joint Center for Artificial Photosynthesis, Lawrence Berkeley National Laboratory, Berkeley, California, USA

[3]Energy Storage and Distributed Resources Division, Lawrence Berkeley National Laboratory, Berkeley, California, USA

Correspondence
Alexis T. Bell, Department of Chemical and Biomolecular Engineering, University of California Berkeley, Berkeley, California 94720, USA.
Email: alexbell@berkeley.edu
Adam Z. Weber, Joint Center for Artificial Photosynthesis, Lawrence Berkeley National Laboratory, Berkeley, California 94720, USA. Email: azweber@lbl.gov

Abstract

Commercial-scale generation of carbon-containing chemicals and fuels by means of electrochemical CO_2 reduction (CO_2R) requires electrolyzers operating at high current densities and product selectivities. Membrane-electrode assemblies (MEAs) have been shown to be suitable for this purpose. In such devices, the cathode catalyst layer controls both the rate of CO_2R and the distribution of products. In this study, we investigate how the ionomer-to-catalyst ratio (I:Cat), catalyst loading, and catalyst-layer thickness influence the performance of a cathode catalyst layer containing Ag nanoparticles supported on carbon. In this paper, we explore how these parameters affect the cell performance and establish the role of the exchange solution (water vs. $CsHCO_3$) behind the anode catalyst layer in cell performance. We show that a high total current density is best achieved using an I:Cat ratio of 3 at a Ag loading of 0.01–0.1 mg_{Ag}/cm^2 and with a 1.0 M solution of $CsHCO_3$ circulated behind the anode catalyst layer. For these conditions, the optimal CO partial current density depends on the voltage applied to the MEA. The work also reveals that the performance of the cathode catalyst layer is limited by a combination of the electrochemically active surface area and the degree to which mass transfer of CO_2 to the surface of the Ag nanoparticles and the transport of OH^- anions away from it limit the overall catalyst activity. Hydration of the ionomer in the cathode catalyst layer is found not to be an issue when using an exchange solution. The insights gained allowed for a Ag CO_2R MEA that operates between 200 mA/cm^2 and 1 A/cm^2 with CO faradaic efficiencies of 78–91%, and the findings and understanding gained herein should be applicable to a broad range of CO_2R MEA-based devices.

KEYWORDS
catalyst layer, CO_2 reduction, electrolyzer, I:C, ionomer, membrane-electrode assembly

1 | INTRODUCTION

Electrochemical CO_2 reduction (CO_2R) offers a versatile option for converting CO_2 to chemical feedstocks and fuels using renewable energy (e.g., solar, wind). Key to achieving industrial-scale CO_2R is the development and fundamental understanding of a cell that can efficiently and selectively produce value-added CO_2R products. Specifically, a CO_2R electrolyzer must operate at current densities in excess of 200 mA/cm^2 under moderate applied cell potentials (<4 V) to minimize capital costs and achieve high energy efficiency.[1] Prior studies have shown that these targets can be best achieved with a membrane-electrode assembly (MEA) (i.e., a zero-gap cell) because of its efficiency advantages stemming from low ohmic resistance and improved mass transport compared to traditional planar electrode and aqueous gas-diffusion-electrode (GDE) cells with aqueous electrolytes.[2–10]

Figure 1 illustrates the structure of an MEA for the electrochemical reduction of CO_2 to CO and H_2. The cathode is composed of a catalyst layer (CL) deposited onto a microporous layer (MPL) residing on top of a gas-diffusion layer (GDL), while the anode is composed of a CL deposited onto a porous transport layer (PTL). The cathode CL consists of carbon-supported silver (Ag) nanoparticles, while the anode CL consists of unsupported iridium/iridium oxide (Ir/IrO$_2$) nanoparticles. An anion-conducting polymer is used between the electrodes because prior findings have demonstrated that lower hydrogen-evolution-reaction (HER) rates correlate with the lower proton availability that is observed in high pH environments for Ag cathodes; these conditions enhance carbon-monoxide evolution.[11–16] Specifically, the anion-exchange membrane (AEM) enables the transport of hydroxide (OH$^-$) anions produced at the cathode via CO_2R and HER (see Equations 1 and 2) to the anode, where they are consumed via the oxygen-evolution reaction (OER) (see Equation 3). For similar reasons, the catalyst particles at both electrodes are covered with a solid-state anion-conducting ionomer. We note that homogeneous buffer reactions occur in the hydrated ionomer and membrane (see Equations 4 and 5), which lead to the formation of HCO$_3^-$ and CO$_3^{2-}$ that are transported across the membrane, essentially pumping CO_2 from the cathode to the anode and representing a major loss in the utilization of CO_2.[2] Three MEA designs were explored in this study: one in which a humidified stream of CO_2 was supplied to the cathode and a humidified stream of N_2 was supplied to the anode (i.e., Full-MEA), the second design consisting of a humidified stream of CO_2 supplied to the cathode and liquid H_2O recirculating behind the anode (i.e., H_2O-MEA), and

a third design that is similar to the second except that an ionic solution (CsHCO$_3$) was recirculated behind the anode (i.e., Exchange-MEA). CsHCO$_3$ was chosen as the ion solution because it can supply hydrated Cs$^+$ cations to the cathode CL, which have been shown to enhance the rate of CO_2R over Ag relative to other alkali metal cations.[17] Bicarbonate (HCO$_3^-$) was chosen as the anion, rather than hydroxide, to avoid significant loss of CO_2 due to the aforementioned CO_2 pumping phenomenon.[2] The half and buffer reactions occurring at each side of this device are

$$\text{Cathode} - \text{COER} : CO_2 + H_2O + 2e^-$$
$$\rightarrow CO + 2OH^- \quad (U° = -0.11 \text{ V vs. SHE}) \quad (1)$$

$$\text{Cathode} - \text{HER} : 2H_2O + 2e^-$$
$$\rightarrow H_2 + 2OH^- (U° = -0.828 \text{ V vs. SHE}) \quad (2)$$

$$\text{Anode} - \text{OER} : 4OH^-$$
$$\rightarrow O_2 + 2H_2O + 4e^- \quad (U° = 0.401 \text{ V vs. SHE}) \quad (3)$$

$$CO_2 + OH^- \leftrightarrow HCO_3^- (pK_a = 6.37) \quad (4)$$

$$HCO_3^- + OH^- \leftrightarrow CO_3^{2-} + H_2O \ (pK_a = 10.3) \quad (5)$$
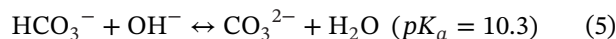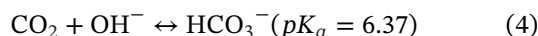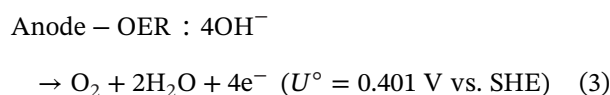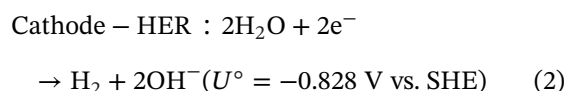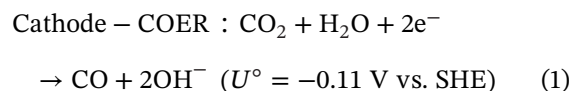
The total current density (TCD) and product distribution obtained with an MEA used for CO_2R depend on a number of interrelated factors, such as membrane and ionomer hydration, cell temperature, reactant partial pressure, *etc*. Prior research has shown that the distribution of CO_2R products is a strong function of both the catalyst composition and its surrounding microenvironment.[2,3,11,18,19] In the case of an MEA, the ionomer-to-catalyst (I:Cat) ratio, catalyst loading, and thickness of the CL also impact cell performance.[20,21] However, the effect of all these design factors on CO_2R is not yet fully understood. In the present study, we conducted a systematic investigation of the effect of these parameters on the activity and product distribution of a CO_2R MEA using a Ag cathode. Ag is of particular interest as an electrocatalyst because it produces only H_2 and CO, a product mixture that can be readily converted to a spectrum of hydrocarbons via Fischer-Tropsch synthesis.[22,23] Tandem systems that convert CO_2 to CO and subsequently convert CO to C$_{2+}$ products using Ag-Cu electrodes[24,25] can also benefit from this study in terms of informing their system designs to maximize CO production.[26]
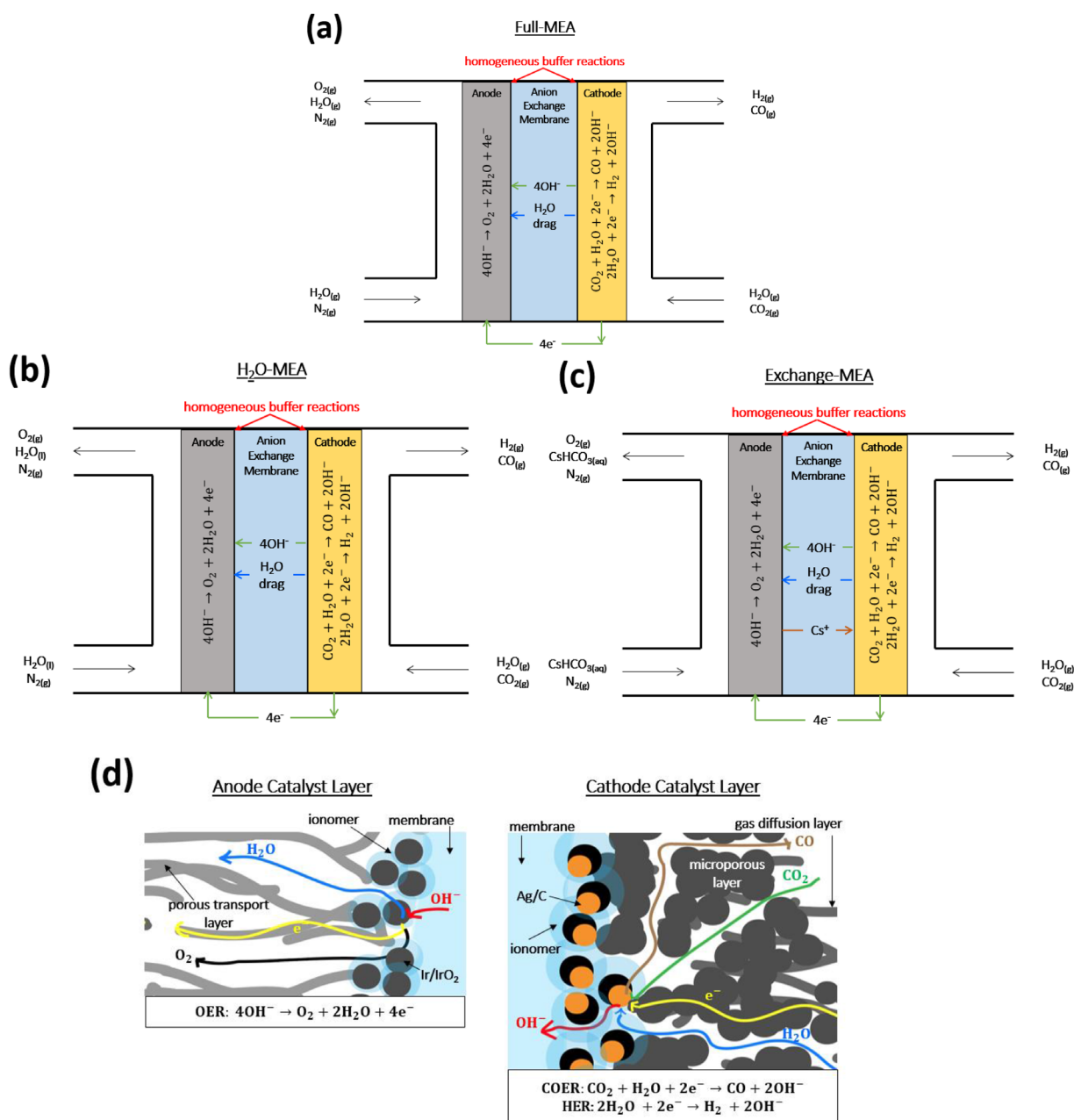
FIGURE 1 Schematics of the ionomer-catalyst-membrane microenvironment in a Ag cathode, Ir anode CO_2 reduction MEA system: (a) Full-MEA schematic, (b) H_2O-MEA schematic, (c) Exchange-MEA schematic, and (d) Blow ups of the cathode and anode catalyst layers. The schematics provide a system-wide overview of the MEA device for Ag CO_2R with associated reactants and products. Homogenous buffer reactions, electroosmotic water drag, and migration of exchange solution cations occur in the device

2 | EXPERIMENTAL METHODS

2.1 | Catalyst inks and electrode substrates

The Ag cathode ink comprised Ag/C particles (i.e., 20% Ag on a Vulcan XC-72 carbon support, Premetek®), Sustainion® ionomer (5% in ethanol, Dioxide Materials®), water (Milli-Q®, 18 mΩ), and n-propanol (Sigma–Aldrich®). The Ir anode catalyst ink comprised IrO_2

nanoparticles (Tanaka®, SA = 100), Sustainion® ionomer (at an optimal ionomer content of 11.6 wt.-%)[27], water, n-propanol, and ethanol (Sigma–Aldrich®). Detailed ink recipes are provided in Table S1. The inks were sonicated ultrasonically (Symphony® Sonicator) for 30 min.

The cathode electrode substrate consisted of a microporous layer (MPL) covering a gas-diffusion layer (GDL) made of carbon fibers and 5 wt.-% PTFE and with a total composite porosity of 0.52 (Sigracet® 39BC). The anode electrode substrate was a proprietary mesoporous tita-

nium (Ti) porous transport layer (PTL) provided by NEL Hydrogen®. Before deposition, both electrode substrates were cleaned with ultra-pure nitric acid to remove electrochemically active trace impurities.[28] Catalyst inks were then spray-coated onto the cathode and anode substrates using an ultrasonic spray coater (Sono-Tek® Exactacoat). For each electrode, the spray coating time was adjusted to achieve the desired loading. After deposition, each electrode was pretreated in 1 M KOH for at least 24 h to facilitate anion exchange in the ionomer.

2.2 | Membrane and cell assembly

A 50 μm-thick hydrated Sustainion® X37-50 Grade RT membrane (Dioxide Materials®) was pretreated in 1 M KOH for at least 24 h. The membrane was sandwiched between the two prepared electrodes, and the resulting MEA was assembled into a 5 cm^2 commercial cell (Fuel Cell Technologies®) (see Figure S1).[29] A torque wrench was used to tighten each cell bolt to 40 in-lb and 10-mil (i.e., 0.01″) thick PTFE gaskets (Fuel Cell Technologies®) were used on each gas channel to ensure reproducible and uniform compression across the MEA and to prevent leakages. The cell was then connected to a potentiostat with a 10A booster (Bio-Logic®).

The CO_2 entering the cathode compartment was humidified by bubbling it through a bottle of deionized water (Milli-Q®, 18 mΩ) maintained at 50°C via a hot-water bath. A flow of deionized water (Milli-Q®, 18 mΩ) or cesium bicarbonate ($CsHCO_3$) (Sigma–Aldrich®) at 50°C was fed behind the anode as the MEA exchange solution (see Figure S2). The MEA cell was heated and operated at 50°C. The cathode feed flow rate was set to or above 200 mL min^{-1} of humidified CO_2 (measured using a mass-flow controller (Alicat Scientific®)) to avoid reactant supply limitations and mass-transfer effects stemming from large fractional conversions. The exchange solution fed behind the anode was rapidly circulated (24.6 mL min^{-1}) using a peristaltic pump (Masterflex®) so that concentrations in the gas channels and porous electrodes remained uniform and gradients were minimized. Flow rates of the cathode and anode outlet gases were verified using a mass-flow meter (MFM) (Alicat Scientific®) to ensure no leakage across the entire system and for faradaic-efficiency (FE) calculation purposes.

2.3 | Electrochemical testing

The cell was first monitored at open circuit for 30–60 min to ensure thermal uniformity and complete hydration of

the cell membrane and the ionomer in the CLs. After equilibration, electrochemical-impedance spectroscopy (EIS) was used to measure the high-frequency resistance (HFR, 1 Hz to 1000 kHz) of the cell (which was consistently under 0.2 Ω or 1 Ω cm^2 for all experiments). After these baseline tests were completed, chronoamperometry (CA, constant-voltage hold) was performed together with in-line gas chromatography (GC) analysis (SRI Instruments®) using both a flame-ionization detector and a thermal-conductivity detector. A polarization curve was obtained, where each voltage step of 0.4 V was held for at least 30 min. For each voltage step, the reported current density was averaged over the last 15 min. Two GC samples were taken per electrode: the measured CO and H_2 product concentrations, the corresponding current density, and the outlet flow rate were used to determine the product FE at each voltage step. Error bars denote multiple separate measurements with different MEAs.

3 | RESULTS & DISCUSSION

3.1 | System design choice

Exploratory experiments conducted at the outset of this work established that in order to ensure adequate hydration of the ionomer and the membrane, the MEA should be operated as either an H_2O-MEA or an Exchange-MEA. As seen in Figure S3, operation of the MEA as a Full-MEA increases the cell voltage required to achieve a given current density, and this problem becomes more severe at higher current densities, with poorer stability (i.e., larger hysteresis between voltage sweeps) demonstrated in the Full-MEA compared to the H_2O-MEA. This pattern is believed to be a consequence of the decrease in the ionomer and membrane conductivity as the current density rises, thus leading to dehydration of the polymeric components.[2] Raising the cell temperature of the H_2O-MEA from 25 to 50°C resulted in superior overall performance due to the higher water content and faster kinetics and mass transport at elevated temperatures (see Figure S4). Thus, an H_2O-MEA operated at 50°C was used as the baseline for the following studies.

3.2 | The effect of cathodic I:Cat ratio

The catalyst loading at both the anode and cathode CLs was fixed at 1 mg$_{catalyst}$ cm^2, while the ionomer-to-catalyst (I:Cat) ratio for the cathode CL was varied from 1 to 5 on a weight basis. Table S2 shows how the I:Cat ratio is related to the more often used ionomer-to-carbon (I:C)
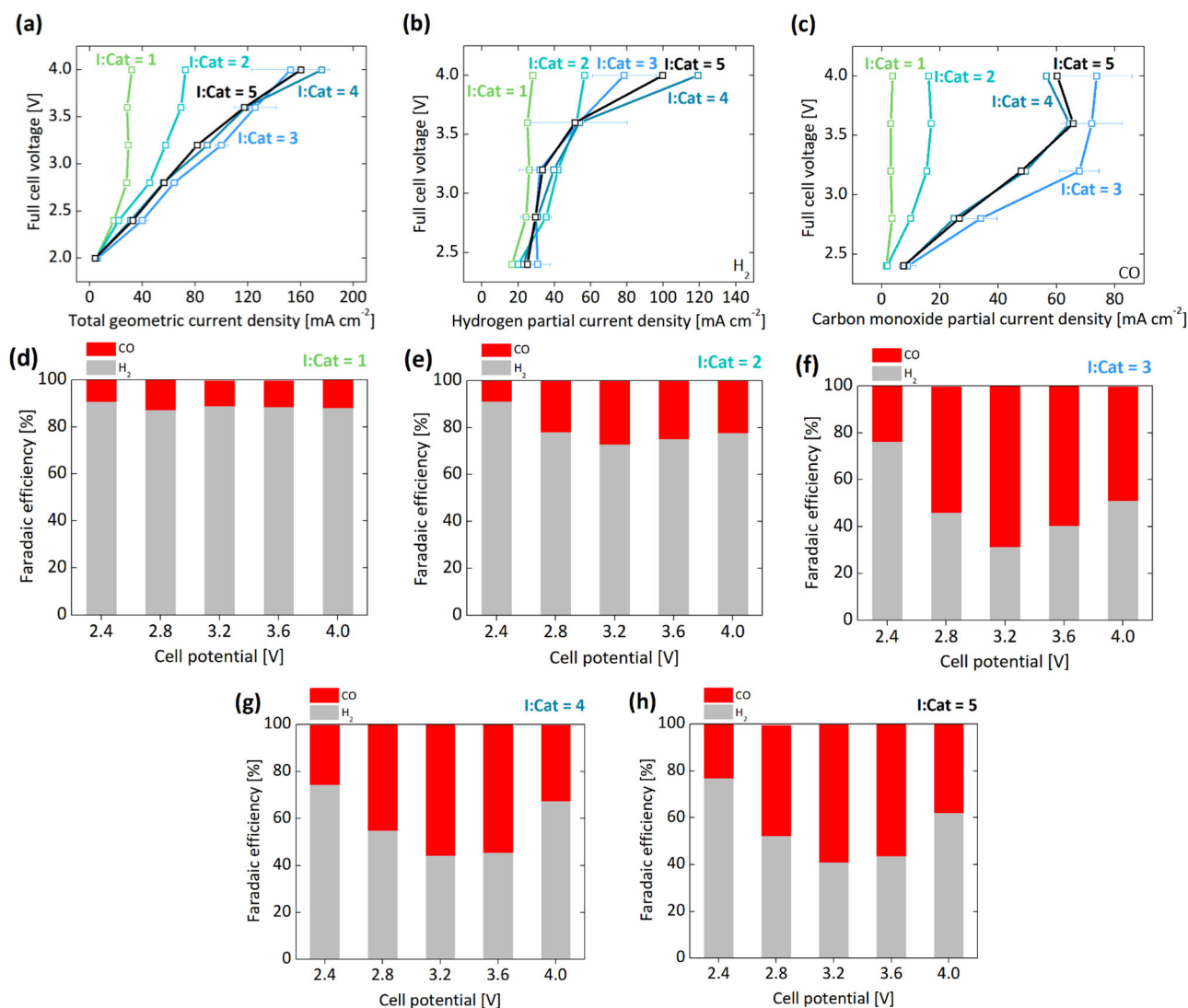
FIGURE 2 Polarization (a), hydrogen partial current density (b), and carbon monoxide partial current density (c) behavior as a function of the cathodic ionomer-to-catalyst ratio. Faradaic efficiency as a function of potential for different ratios: I:Cat = 1 (d), I:Cat = 2 (e), I:Cat = 3 (f), I:Cat = 4 (g), I:Cat = 5 (h) in a Ag cathode, Ir anode MEA. Test conditions: 50°C, atmospheric pressure, 200 mL min^{-1} fully humidified CO_2 feed at the cathode, liquid water behind the anode

ratio presented in the fuel-cell literature, but that metric is less relevant here since carbon is not always necessarily present in the CL.

Polarization curves for different cathode CL I:Cat ratios presented in Figure 2a demonstrate that, for a given cell potential, the TCD increases as the I:Cat increases from 1 to 3, with I:Cat ratios from 3 to 5 exhibiting nearly identical behavior. Figure 2b and c display how the I:Cat ratio impacts the partial current densities for H_2 and CO, respectively. As I:Cat increases from 1 to 3, the partial current density for H_2 increases monotonically, whereas for CO, the partial current density increases up to an I:Cat ratio of 3 and then decreases for higher I:Cat ratios, especially once the cell potential increases above 3.5 V. The observed trends in the partial current densities of H_2 and CO with

the I:Cat ratio and cell potential lead to an increase in the FE for CO and a decrease in the FE for H_2, as seen in Figure 2d-h. For I:Cat = 1, the FE for both products is relatively insensitive to the cell potential, whereas for the other I:Cat ratios, the CO FE reaches a pronounced maximum at 3.2 V, especially for I:Cat = 3. Furthermore, the CO partial current levels off with increasing cell potential for I:Cat = 2 and 3, whereas the H_2 partial current rises monotonically with increasing I:Cat. A CO FE (68%) and partial current (74 mA/cm^2) are observed for I:Cat = 3 at 3.2 V. Analysis of product selectivity at constant current (i.e., fixed OH$^-$ flux) as given in Figure S5a-c demonstrates that I:Cat = 3 still yields both a high CO partial current and FE, and these characteristics are lower for the higher I:Cat = 4 and 5 systems.
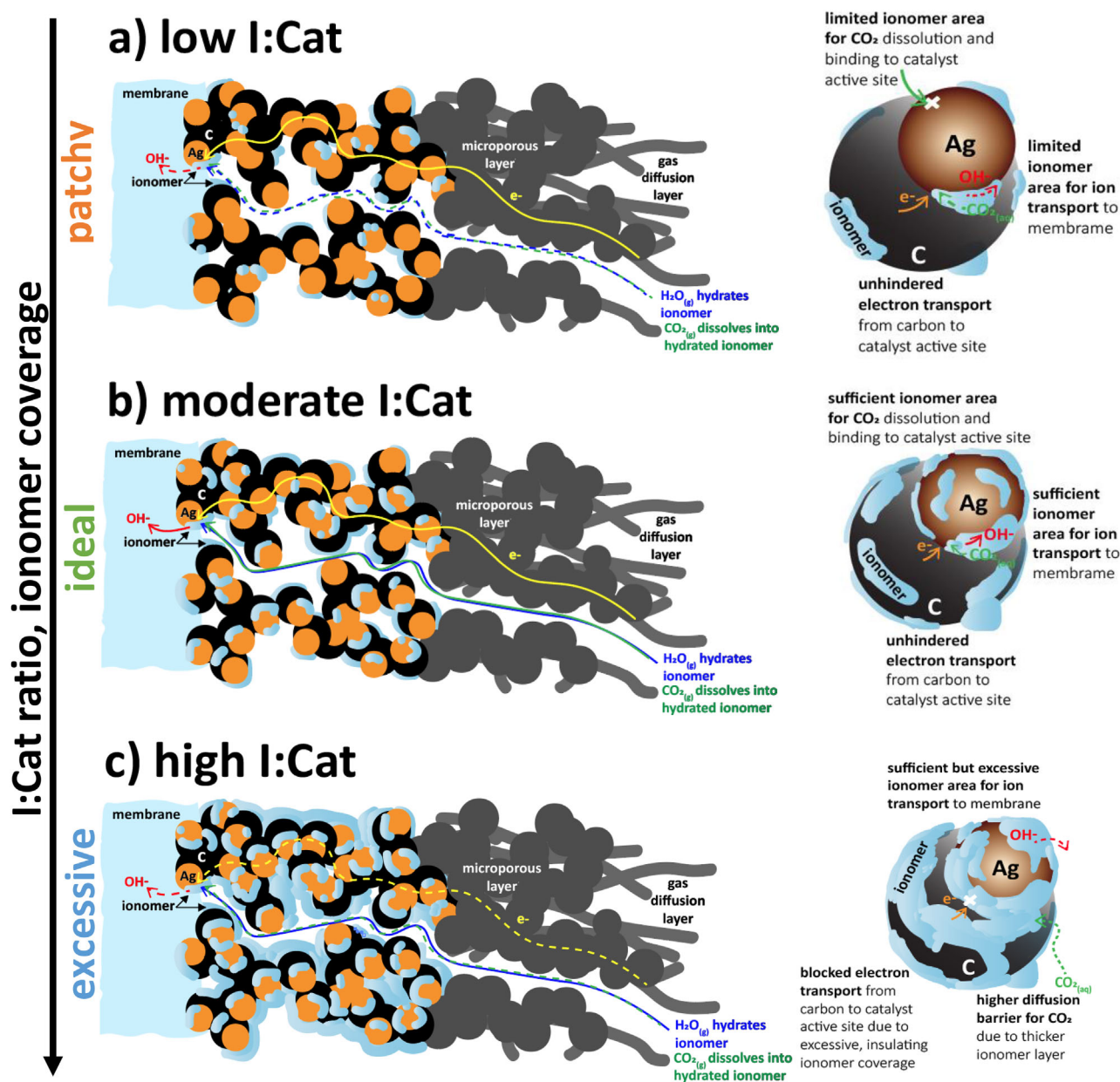
6 of 13   **Electrochemical Science Advances**   RESEARCH ARTICLE
doi.org/10.1002/elsa.202100186

Chemistry
Europe
European Chemical
Societies Publishing

FIGURE 3   Schematic of the catalyst-layer microenvironment and ionomer-catalyst distribution on a catalyst and support nanostructure based on the I:Cat ratio and ionomer content/coverage. The patchy ionomer distribution depicts low I:Cat $\leq$ 2, the excessive distribution depicts high I:Cat $\geq$ 4, and the idealized distribution refers to moderate I:Cat = 3. Electron, ion, and gaseous pathways and tradeoffs are also shown

Figure 3 illustrates our conceptual picture of the cathode CL structure. The electrochemically active surface area (ECSA) refers to the surface area of Ag covered by ionomers for which there are accessible ionic and electronic pathways to the membrane and GDL, respectively. For CO_2R to occur on the Ag/C catalyst particles, it is essential that percolation pathways exist for electron flow from the cathode GDL to the Ag/C particle, for OH^- transport from the ionomer covering the Ag nanoparticles to the membrane, and for gas transport from the flow channel to the catalytically active sites. The pathway for electron flow

is provided by good contact of the carbon particles supporting the Ag nanoparticles with the carbon in the MPL and GDL. The pathway for OH^- anions produced at the cathode is via continuous ionomer tendrils connecting the surface of the Ag particles to the membrane. If the void space in the cathode CL is partially filled with liquid electrolyte (originating from the anode exchange solution), then this medium can also act as a pathway for OH^- transport, as occurs in the wetted pores of an aqueous GDE.[10] The existence of parallel pathways for ion transport from the catalyst surface to the membrane implies that the microenvi-

7 of 13   **Electrochemical Science Advances**   RESEARCH ARTICLE
doi.org/10.1002/elsa.202100186

Chemistry
Europe
European Chemical
Societies Publishing

ronment in the CL and near the catalyst surface can be heterogeneous. Finally, the transport of CO_2 occurs from the flow channel on the cathode side of the MEA, through the pores in the GDL and MPL, and to the Ag/C catalyst particles. To reach the Ag surface, gaseous CO_2 must dissolve into a thin layer of ionomer or liquid electrolyte covering the Ag catalyst particles.

The cartoons in Figure 3 illustrate how the structure of the cathode CL changes for cases of low, moderate, and high I:Cat ratios. For each case, the right side illustrates the specific coverage of the Ag/C nanoparticle and the supporting ionomer, whereas the left side illustrates the electronic, ionic, and pore-space connectivity throughout the CL. As the I:Cat ratio increases, the fraction of individual Ag/C particles covered with ionomer increases. For a H_2O-MEA, increasing the ionomer coverage of the Ag particles increases its ECSA since the ionomer provides access for H_2O and CO_2 to the Ag surface and a path for the movement of OH^- anions from the Ag surface.

It should be noted that sufficient ionomer must be present so that a bridge develops between the individual Ag/C particles and the membrane since this bridge is essential for the flow of OH^- anions from the CL to the membrane. If these ionomer tendrils are insufficient in number, as in the case of low I:Cat ratios, then the existing ones must carry all of the ion current, inducing local mass-transport limitations of OH^- and consequently low ion conductivity.[30] For the low number of active sites, the high current density in the tendrils coupled with their low conductivity can lead to ohmic heating that has the potential to dehydrate the CL. This loss due to ohmic heating is offset by the water flux through the membrane and into the ionomer tendril provided by the liquid H_2O present behind the anode. Figure S6 depicts an ionomer dehydration model of how the cathode CL water activity changes with the current density and I:Cat ratio. The results of the model clearly show that extensive ionomer dry-out (i.e., water activity falling well below 1.0) is not at all expected to occur in the cathode CL, especially in portions closest to the membrane (i.e., the active thickness of the CL) at the current densities measured due to the existence of the water from the exchange solution. We note that low coverage of the Ag nanoparticles by the ionomer reduces the ECSA, an issue that is particularly important in the case when the MEA operates with only water behind the anode CL.

The very steep rise in the cell voltage with TCD seen in Figure 2a for I:Cat ratios of 1 and 2 depicts limiting-current behavior that is attributed to both low ECSA and mass-transport limitations within the cathode CL. As noted above, patchy coverage of the Ag particles by ionomers at low I:Cat ratios reduces the active area for catalysis. This means that the overpotential applied to these particles rises more sharply than would be anticipated, resulting in severe local mass-transfer limitations of CO_2, which accesses the surface of the Ag particles primarily via transport through the ionomer tendrils. Moreover, the pH in the portion of the tendrils close to the Ag/C nanoparticles increases due to the higher local reaction rate, causing a decrease in the local concentration of CO_2 due to its consumption by buffering reactions, as described above (see Equations 4 and 5).

Upon increasing the I:Cat ratio to 3, more of the Ag/C particles become covered by ionomer, which in turn increases the number of ionomer tendrils available to carry the ionic current. These changes result in an overall higher rate of CO_2R, as evidenced by the increased CO partial currents and FEs shown in Figure 2c-f. The proposed interpretation of the effects of the I:Cat ratio is in agreement with previous studies of local conditions in CO_2R systems.[31][11–16] For an I:Cat ratio = 3 to 5, the current carrying capacity of the ionomer tendrils no longer limits the TCD, as evidenced by the polarization curves becoming more ohmic in character (i.e., exhibiting a linear relationship between current and potential). However, if the I:Cat ratio is raised above 5, the extra ionomer decreases the CL porosity (see Figure S7) and can interfere with electron conduction from the cathode MPL and GDL to the Ag/C particles and with the passage of CO_2 to the Ag/C particles. Under these conditions, the cell potential for a given TCD is expected to again rise.

Figure 3 also helps rationalize the changes in the partial current densities for H_2 and CO seen in Figure 2b and c. Simulations of Ag MEAs have shown that the product partial current densities are very sensitive to the overpotential at the Ag particles that drive CO_2R.[2] In the present study, the composition and structure of the anode CL remain fixed as the I:Cat ratio of the cathode CL increases. Since the anode CL is in intimate contact with liquid water, it is reasonable to assume that the ionomer in the anode CL remains fully hydrated, as does the membrane. Under these constraints, the overpotential due to anode kinetics should be independent of the I:Cat ratio for the cathode CL and should only depend on the TCD. Likewise, if the membrane remains fully hydrated, its conductivity will not change significantly, and hence, the ohmic loss across the membrane should increase linearly with the current density. Moreover, CO_2 can be lost due to buffer reactions involving OH^-, which produce HCO_3^- and CO_3^{2-}. As noted above, the latter process becomes increasingly severe as the extent of mass-transfer resistance increases at high TCD since OH^- is produced in direct proportion to the current. For I:Cat = 1 and 2, the number of ionomer tendrils connecting the Ag/C particles to the membrane is low, resulting in a relatively low cathode overpotential and subsequently mainly H_2 production.[32] When the I:Cat ratio increases to 3, there is now a sufficient number of

8 of 13   **Electrochemical Science Advances**   RESEARCH ARTICLE
doi.org/10.1002/elsa.202100186

Chemistry
Europe
European Chemical
Societies Publishing

ionomer tendrils to carry the current even at high current densities. Under these conditions, the cathode overpotential shifts to more positive values, thereby increasing the CO partial current density and FE. However, for yet higher current densities, mass-transfer effects start to set in, causing a decrease in the local CO_2 concentration due to the homogeneous buffer reactions, and consequently, the CO partial current density does not rise as rapidly as that of H_2: the CO FE decreases as a result. When the I:Cat ratio rises to 4 and 5, the effects of CO_2 and OH^- transfer limitations are expected to become more significant because of thicker ionomer layers covering Ag/C particles.

These same I:Cat ratio trends were observed experimentally for the case of H_2O electrolysis (i.e., HER-only at the cathode) in a H_2O-MEA containing an Ir anode CL and a Ag/C CL (see Figure S8). An I:Cat of 3 was again found to be best, suggesting that the CL structure (and perhaps associated water- and ion-transport limitations) dominates performance. The findings are consistent with the data of Xu et al.,[33] who characterized the CL microstructure by scanning electron microscopy (SEM) and nanometer-scale X-ray computed tomography (nano-XCT), which revealed that larger aggregates of ionomer-catalyst-carbon are formed with excessive ionomer amounts, resulting in a decrease in the ECSA.[33] It is important to note that several complexities and considerations arise when trying to link macroscale device performance to microscale ionomer-catalyst binding and distribution[21] and that, across a range of ionomer types and equivalent weights, changing the ionomer content or I:C ratio also influences the uniformity, morphology, and transport resistances of the CL.[34] Finally, the preferred I:Cat ratio of 3 found in our study (i.e., an I:Cat of 3 corresponds to an I:C of 0.75 (see Table S2)) agrees with what was found for a proton-exchange-membrane fuel cell, where the preferred I:C ratio was close to 1.[35]

3.3 | Effect of exchange-solution concentration

Previous studies have shown that adding an electrolyte behind the anode of an MEA improves the TCD obtained for a given cell potential relative to what is observed using pure water.[36–41] In this study, $CsHCO_3$ was added to the water circulated behind the anode CL, effectively producing an Exchange-MEA. For these experiments, the cathode CL I:Cat was 3 and the catalyst loading was 1 mg_{Ag}/cm^2.

The addition of $CsHCO_3$ to the water fed behind the anode of the MEA has a noticeable impact on the TCD, as shown in Figure 4a, especially for concentrations approaching 1 M where current densities approach 1 A/cm^2. The increase in current density for a given applied

potential is particularly significant above a cell potential of 2.5 V. These effects on the TCD are attributed to the creation of additional OH^- conduction pathways through the pores in the cathode CL (see Figure 3), which provide parallel pathways to the ionomer tendrils between the Ag/C particles and the AEM. We note that the migration of cations from the electrolyte behind the anode to the cathode CL through AEMs at high current densities has been predicted in simulations of Exchange-MEAs[2] and experimental studies have observed salt precipitation at the cathode when the electrolyte concentration exceeds its solubility limit.[42] As the ion concentration behind the anode increases, Donnan exclusion from the membrane is overcome, and Cs^+ and HCO_3^- ions can now be transported across the membrane. The creation of an electrolyte conduction pathway within the CL also increases the ECSA and improves CL utilization. These effects are consistent with the increased partial current density for CO and H_2 observed at higher cell potentials. A similar impact of electrolyte has been reported for hydroxide-exchange-membrane water electrolyzers,[43] where the additional liquid-based ionic pathway becomes more favorable than the ionomer pathway as the exchange-solution ion concentration increases, further contributing to an increase in the ECSA.

The selectivity trends shown in Figure 4b–g are attributed to the effect of the cathode overpotential coupled with the effect of CO_2 and OH^- transport at higher applied potentials. The presence of Cs^+ cations at the electrolyte/Ag interface and at a similar interface beneath the Sustainion® ionomer also enhances the activity of Ag for CO_2R because the accumulation of hydrated Cs^+ cations on the catalyst surface has been shown to strengthen the electrostatic field in the double layer and thereby enhance CO_2 adsorption.[17,44] Furthermore, since the bicarbonate ion has a lower pKa than water, at higher concentrations in the CL, it becomes a significant proton donor supply and buffering agent, which reduces the local pH and promotes HER.[45,46] In addition, when HFR EIS was conducted for the MEA and operated at a fixed current density of 500 mA/cm^2 with a 0.5 M or a 1 M $CsHCO_3$ solution behind the anode catalyst layer, the total resistance measured was 0.14 Ω and 0.13 Ω, respectively. In contrast, within its current density range, the resistance of the H_2O-MEA system was just under 0.2 Ω. Thus, ohmic resistance was not a controlling factor in the performance of the Exchange-MEA. These various effects are coupled and not readily deconvoluted without additional advanced characterization techniques or mathematical models that are beyond the scope of the current study. The effects of the applied cell potential on the partial current densities and the FE for CO are qualitatively similar to those seen in Figure 2 but are more dramatic. While the CO FE is highest
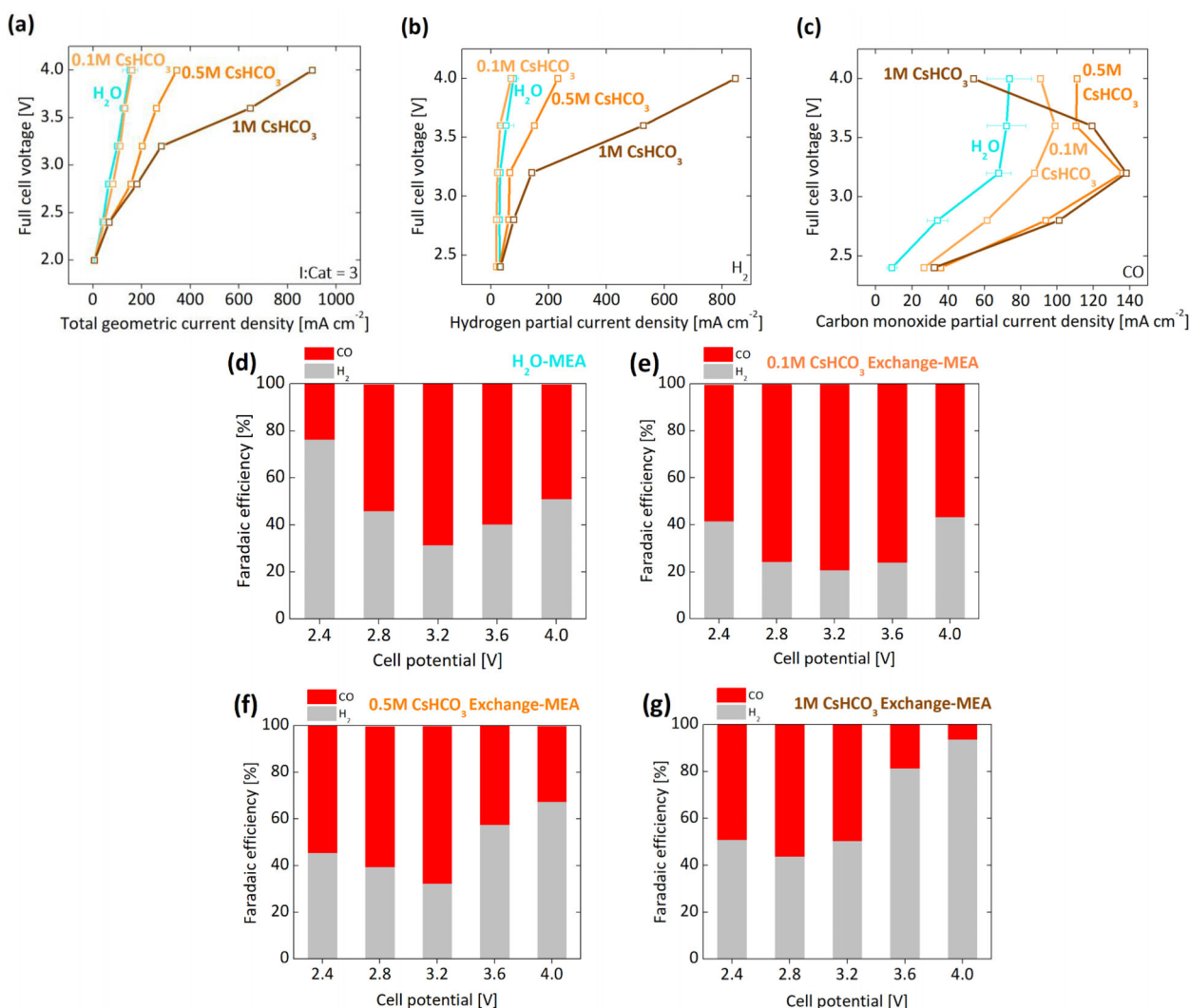
FIGURE 4 Polarization (a), hydrogen partial current density (b), and carbon monoxide partial current density (c) behavior as a function of exchange-solution concentration. Faradaic efficiency as a function of potential for the different concentrations: H_2O-MEA (d), 0.1 M $CsHCO_3$ (e), 0.5 M $CsHCO_3$ (f), and 1 M $CsHCO_3$ (g) in a Ag cathode, Ir anode MEA. Test conditions are the same as those in Figure 2 except that the cathodic I:Cat was fixed at 3 (weight basis) and that liquid water or $CsHCO_3$ was circulated behind the anode

(79%) for 0.1 M $CsHCO_3$ Exchange-MEA (see Figure 4e), the CO partial current density is highest for 0.5 and 1 M $CsHCO_3$ (i.e., CO partial current densities >100 mA/cm², see Figure 4c). Furthermore, for a constant current density, the CO partial current density for the 1 M $CsHCO_3$ system is higher than that for 0.5 M $CsHCO_3$. These observations reinforce why FE trends are an insufficient basis for judging CO_2R performance and why it is also important to look at the CO partial current density.[47,48]

3.4 | The effect of catalyst loading and CL thickness

As noted above, substitution of water by a $CsHCO_3$ solution enhances the activity of the Ag/C particles in the cath-

ode CL and reduces the net resistance of the CL to anion transport. The next question explored was the effect of changing the number of active sites by changing the catalyst mass loading (mg_{Ag}/cm^2) and, hence, the thickness of the cathode CL. These experiments were carried out with a fixed Ag-to-carbon ratio (Ag/C) of 20 wt.%, a cathodic I:Cat = 3, and a 1 M $CsHCO_3$ exchange solution behind the anode.

Figure 5a–c shows the effect of catalyst loading on the TCD and the partial currents for H_2 and CO. Decreasing the Ag loading from a nominal value of 1 to 0.1 mg_{Ag}/cm^2 did not significantly alter the TCD over the whole range of cell potentials. However, when the loading was further reduced to 0.01 mg_{Ag}/cm^2, the TCD exhibited similar limiting-current behavior to that seen when the I:Cat ratio was reduced from 3 to 1 (see Figure 2a). This pattern
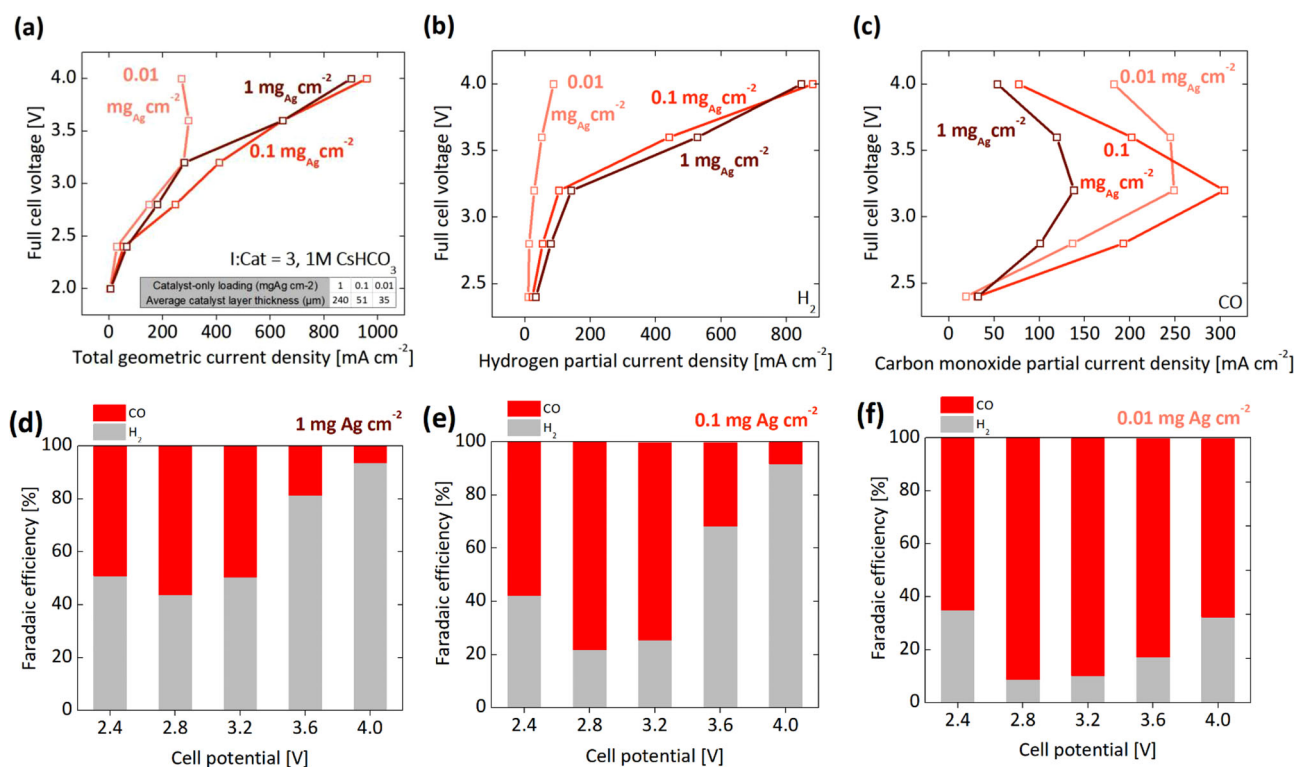
FIGURE 5 Polarization (a), hydrogen partial current density (b), and carbon monoxide partial current density (c) behavior as a function of Ag catalyst loading. Faradaic efficiency as a function of potential for the different loadings: 1 mg_{Ag}/cm^2 (d), 0.1 mg_{Ag}/cm^2 (e), 0.01 mg_{Ag}/cm^2 (f) in a Ag cathode, Ir anode MEA. Test conditions are the same as those in Figure 2 except that the cathodic I:Cat was fixed at 3 (weight basis) and 1 M $CsHCO_3$ was circulated behind the anode. A pressure-sensing Mitutoyo® micrometer was used to obtain the catalyst-layer thickness measurements shown in the inset table in (a)

suggests that the most active part of the CL is that located near the membrane surface, consistent with earlier studies of CO_2R in an MEA system.[32,49,50] One of these studies[32] revealed that the cathode potential on the Ag particles in the cathode CL became significantly more positive with increasing distance from the CL/membrane interface as a consequence of the increasing resistance to OH⁻ mass transfer. Consistent with this reasoning, Figure 5a suggests that only approximately 10% of the CL layer at a catalyst loading of 1 mg_{Ag}/cm^2 is actually active (i.e., ~20 μm). Further reduction of the Ag loading to 0.01 mg_{Ag}/cm^2 reveals that if the loading is too low, the current that needs to be supplied by each particle in the CL rises, resulting in an increase in mass-transport limitations to and from the catalyst surface due to the decreased ECSA, as well as a reduction in the availability of conduction pathways via the electrolyte in the pores of the CL due the smaller CL volume (at fixed I:Cat) having reduced contact sites of the electrolyte with ionomer tendrils and Ag/C particles. These phenomena help explain the observed sudden rise in the cell potential required to achieve current densities of more than ~250 mA/cm^2.

It is notable that reducing the catalyst loading from 1 to 0.1 mg_{Ag}/cm^2 does not have a large effect on the

partial current density for H_2 but results in a substantial increase in the partial current density and FE for CO. For cell potentials below the optimal 3.2 V, in which the TCD is essentially independent of Ag loading, the partial current density for CO increases as the Ag loading decreases but remains largely unchanged from 0.1 to 0.01 mg_{Ag}/cm^2. However, the CO FE greatly increases over this same loading range (i.e., a CO FE of 78% was attained at 0.1 mg_{Ag}/cm^2, and a very high CO FE of 91% was attained at 0.01 mg_{Ag}/cm^2 at 3.2 V). This is not due to a particularly large increase in the CO partial current density but rather due to a significant decrease in the H_2 partial current density. For each loading, the CO partial current density goes through a broad maximum, while the H_2 partial current density increases monotonically as the overpotential increases. A constant-current comparison of the selectivity data (see Figure S5g–i) also shows this maximum in CO partial current density as a function of Ag loading, especially for 0.1 mg_{Ag}/cm^2. We believe that this is attributable to the higher cathode overpotential preferentially shifting the product selectivity to products with larger transfer coefficients.[32] For Ag, the product with the larger transfer coefficient is CO ($\alpha_{COER} = 0.44$ and $\alpha_{HER} = 0.36$).[10] It is also notable that decreasing the catalyst loading to 0.01

mg_{Ag}/cm^2 dramatically decreases the partial current density for H_2 but has a much more modest effect on the partial current density to CO. This pattern may reflect a lower H_2O/CO_2 ratio at the catalyst surface.

4 | CONCLUSIONS

This work explored the role of the cathodic ionomer-to-catalyst (I:Cat) ratio, catalyst loading, catalyst-layer thickness, and anode exchange-solution concentration in CO_2 reduction (CO_2R) for a membrane-electrode assembly (MEA) containing supported Ag/C catalysts at the cathode. The aim of this work was to understand the influence of these parameters on the total current density, the rate of CO formation, and the associated faradaic efficiency (FE). We have found that when only water is present in the anode compartment behind the anode CL, both the anion-exchange membrane (AEM) and associated ionomer in contact with the Ag particles are essentially completely hydrated, avoiding dehydration phenomena that can limit catalytic performance. However, the total current density and the CO partial current density are both sensitive to the I:Cat ratio. For I:Cat ratios of 1 and 2, the electrochemically active surface area (ECSA) is low, and the total current density is limited by the mass transport of CO_2 and OH^- through the ionomer tendrils connecting the Ag particles to the AEM. Under these conditions, the OH^- concentration and production rate near the Ag surface are high, which reduces the local concentration of CO_2 due to the reaction with OH^- to produce HCO_3^- and CO_3^{2-}; this results in H_2 being the primary product. For I:Cat ratios of 3 and greater, the ECSA is higher and these mass-transfer limitations are ameliorated at lower total current densities; consequently, CO is produced with greater FE and current density. However, mass-transfer limitations are observed at high current densities. The addition of $CsHCO_3$ to the water in the anode compartment significantly increases the total current density attained for a given applied potential. This is ascribed to the creation of parallel channels for OH^- conduction from the Ag particles via the electrolyte present in the pores of the CL between the ionomer tendrils and the AEM. The presence of electrolyte in the cathode CL also increases the CO partial current density relative to that for H_2, but at high applied potentials where mass-transfer limitations are set in, the CO partial current density decreases relative to that for H_2. The catalyst loading, expressed as milligrams of Ag per square centimeter of cathode area (mg_{Ag}/cm^2), also has an effect on the total current density and the CO partial current density. For an I:Cat ratio of 3 and a $CsHCO_3$ concentration of 1 M, reducing the catalyst loading from 1 to 0.1 mg_{Ag}/cm^2 has little effect on the total current density but increases the CO

FE substantially. A further decrease in the Ag loading to 0.01 mg_{Ag}/cm^2 leads to a significant reduction in the total current density for a given cell potential and a significant reduction in the H_2 partial current density relative to the CO partial current density. The observed effects suggest that for a loading of 1 mg_{Ag}/cm^2, only a tenth of the catalyst is active for CO_2R, but that reducing the loading below 0.1 mg_{Ag}/cm^2 leads to a large loss in ECSA and the onset of significant local mass-transfer limitations; however, the high ratio of CO to H_2 partial currents and very high CO FEs in this latter case cannot be fully explained and warrant further study. Overall, at low enough catalyst loading with constant I:Cat or at low enough I:Cat with constant catalyst loading, the CO_2R MEA system becomes severely limited by low ECSA, poor CO_2 utilization, and mass-transfer limitations.

In summary, the present study illustrates the importance of cathode CL design for achieving high, industrially-relevant total current densities (i.e., 200 mA/cm^2 to 1 A/cm^2) and concurrently high CO FEs (i.e., 78% to 91%), with a recommended range of cathode parameters being catalyst loadings of 0.01 to 0.1 mg_{Ag}/cm^2 with thicknesses on the order of tens of micrometers and with an intermediate I:Cat ratio of 3, as well as a 1 M $CsHCO_3$ anode exchange solution. Our findings also revealed that, despite its solid-state ionomer-based design, under certain operating conditions, the MEA architecture can behave similarly to planar and aqueous GDE cells in their inherent ability to highly tune CO_2R selectivity with their electrode/electrolyte interfaces. This points to an increased possibility of knowledge transfer of fundamental scientific insights from the wider aqueous CO_2R literature across seemingly disparate device systems. Moreover, we find that our interpretations and hypotheses of the effects of catalyst-layer design factors (such as I:Cat, catalyst loading, and catalyst-layer thickness) on performance are largely correlated due to the interrelated nature of the metrics themselves and how a change in one factor can influence the other in the complex and interconnected catalyst-layer microenvironment. These findings not only provide much needed engineering guidance in the form of design factor optimization but also provide foundational scientific insights that improve our understanding of the physical phenomena tradeoffs in CO_2R MEAs and should be readily applicable to a broad range of commercializable CO_2R MEA-based devices.

12 of 13 **Electrochemical Science Advances** | RESEARCH ARTICLE
doi.org/10.1002/elsa.202100186

Chemistry
Europe
European Chemical
Societies Publishing

AUTHOR CONTRIBUTIONS
The manuscript was written through contributions from all authors. All authors approved the final version of the manuscript.

CONFLICT OF INTEREST
The authors declare no conflict of interest.

DATA AVAILABILITY STATEMENT
The data that supports the findings of this study are available in the supplementary material of this article.

REFERENCES

1. J. Sisler, S. Khan, A. H. Ip, M. W. Schreiber, S. A. Jaffer, E. R. Bobicki, C.-T. Dinh, E. H. Sargent, ACS Energy Lett. **2021**, 997.
2. L.-C. Weng, A. T. Bell, A. Z. Weber, *Energy Environ. Sci.* **2019**, *12*, 1950. https://doi.org/10.1039/c9ee00909d.
3. M. R. Singh, E. L. Clark, A. T. Bell, *Phys. Chem. Chem. Phys.* **2015**, *17*, 18924. https://doi.org/10.1039/c5cp03283k.
4. S. Verma, X. Lu, S. Ma, R. I. Masel, P. J. A. Kenis, *Phys. Chem. Chem. Phys.* **2016**, *18*, 7075. https://doi.org/10.1039/c5cp05665a.
5. R. L. Cook, R. C. MacDuff, A. F. Sammells, *J. Electrochem. Soc.* **1990**, *137*, 607. https://doi.org/10.1149/1.2086515.
6. K. Hara, T. Sakata, *Bull. Chem. Soc. Jpn.* **1997**, *70*, 571. https://doi.org/10.1246/bcsj.70.571.
7. D. Kopljar, A. Inan, P. Vindayer, N. Wagner, E. Klemm, *J. Appl. Electrochem.* **2014**, *44*, 1107. https://doi.org/10.1007/s10800-014-0731-x.
8. D. Kopljar, A. Inan, P. Vindayer, R. Scholz, N. Frangos, N. Wagner, E. Klemm, *Chemie-Ingenieur-Technik* **2015**, *87*, 855. https://doi.org/10.1002/cite.201400135.
9. K. Ogura, *J. Electrochem. Soc.* **1999**, *146*, 3736. https://doi.org/10.1149/1.1392542.
10. L. C. Weng, A. T. Bell, A. Z. Weber, *Phys. Chem. Chem. Phys.* **2018**, *20*, 16973. https://doi.org/10.1039/c8cp01319e.
11. S. A. Nitopi, E. Bertheussen, S. B. Scott, X. Liu, K. Albert, S. Horch, B. Seger, I. E. L. Stephens, K. Chan, J. K. Nørskov, T. F. Jaramillo, I. Chorkendorff, *Chem. Rev. 119*, 7610, **2018**, https://doi.org/10.1021/ACS.CHEMREV.8B00705.
12. Y. Hori, R. Takahashi, Y. Yoshinami, A. Murata, *J. Phys. Chem. B* **1997**, *101*, 7075. https://doi.org/10.1021/jp970284i.
13. K. J. P. Schouten, Z. Qin, E. P. Gallent, M. T. M. Koper, *J. Am. Chem. Soc.* **2012**, *134*, 9864. https://doi.org/10.1021/ja302668n.
14. D. Strmcnik, M. Uchimura, C. Wang, R. Subbaraman, N. Danilovic, D. Van Der Vliet, A. P. Paulikas, V. R. Stamenkovic, N. M. Markovic, *Nat. Chem.* **2013**, *5*, 300. https://doi.org/10.1038/nchem.1574.
15. F. S. Roberts, K. P. Kuhl, A. Nilsson, *ChemCatChem* **2016**, *8*, 1119. https://doi.org/10.1002/cctc.201501189.
16. H. Xiao, T. Cheng, W. A. Goddard, R. Sundararaman, *J. Am. Chem. Soc.* **2016**, *138*, 483. https://doi.org/10.1021/jacs.5b11390.
17. J. Resasco, L. D. Chen, E. Clark, C. Tsai, C. Hahn, T. F. Jaramillo, K. Chan, A. T. Bell, *J. Am. Chem. Soc.* **2017**, *139*, 11277. https://doi.org/10.1021/jacs.7b06765.
18. M. R. Gerhardt, L. M. Pant, A. Z. Weber, *J. Electrochem. Soc.* **2019**, *166*, F3180. https://doi.org/10.1149/2.0171907jes.
19. S. Garg, M. Li, A. Z. Weber, L. Ge, L. Li, V. Rudolph, G. Wang, T. E. Rufford, **2020**, https://doi.org/10.1039/c9ta13298h.
20. Z. Taie, X. Peng, D. Kulkarni, I. V. Zenyuk, A. Z. Weber, C. Hagen, N. Danilovic, *ACS Appl. Mater. Interfaces* **2020**, *12*, 52701.
21. S. A. Berlinger, B. D. McCloskey, A. Z. Weber, *ACS Energy Lett.* **2021**, *6*, 2275.
22. O. S. Bushuyev, P. De Luna, C. T. Dinh, L. Tao, G. Saur, J. van de Lagemaat, S. O. Kelley, E. H. Sargent, *Joule* **2018**, *2*, 825.
23. I. Chorendorff, J. W. Niemantsverdriet, *Adsorpt. J. Int. Adsorpt. Soc.* **2003**, *43*, 6586. https://doi.org/10.1002/anie.200461440.
24. Y. Lum, J. W. Ager, *Energy Environ. Sci.* **2018**, *11*, 2935. https://doi.org/10.1039/c8ee01501e.
25. G. Gurudayal, D. Perone, S. Malani, Y. Lum, S. Haussener, J. W. Ager, *ACS Appl. Energy Mater.* **2019**, *2*, 4551. acsaem.9b00791.
26. I. V. Chernyshova, P. Somasundaran, S. Ponnurangam, *Proc. Natl. Acad. Sci. 115*, E9261, **2018**, https://doi.org/10.1073/pnas.1802256115.
27. M. Bernt, H. A. Gasteiger, *J. Electrochem. Soc.* **2016**, *163*, F3179. https://doi.org/10.1149/2.0231611jes.
28. Y. Lum, Y. Kwon, P. Lobaccaro, L. Chen, E. L. Clark, A. T. Bell, J. W. Ager, *ACS Catal.* **2016**, *6*, 202. https://doi.org/10.1021/acscatal.5b02399.
29. V. M. Ehlinger, A. Kusoglu, A. Z. Weber, *J. Electrochem. Soc.* **2019**, *166*, F3255. https://doi.org/10.1149/2.0281907jes.
30. K. H. Kim, K. Y. Lee, H. J. Kim, E. A. Cho, S. Y. Lee, T. H. Lim, S. P. Yoon, I. C. Hwang, J. H. Jang, *Int. J. Hydrogen Energy* **2010**, *35*, 2119. https://doi.org/10.1016/j.ijhydene.2009.11.058.
31. J. C. Bui, I. Digdaya, C. Xiang, A. T. Bell, A. Z. Weber, *ACS Appl. Mater. Interfaces* **2020**, *12*, 52509. https://doi.org/10.1021/acsami.0c12686.
32. L. C. Weng, A. T. Bell, A. Z. Weber, *Energy Environ. Sci.* **2020**, *13*, 3592. https://doi.org/10.1039/d0ee01604g.
33. "Modulation of the microstructure of the Ag/C-based alkaline cathode via the ionomer content for a bipolar membrane fuel cell | Elsevier Enhanced Reader," can be found under https://reader.elsevier.com/reader/sd/pii/S0378775317304834?token=2122C6329F60B8F5BF731A224B9E29F52CBC2055F1FF3FF5D119FB57CCB1952603711EB01748A78C951203BB85DF259A&originRegion=us-east-1&originCreation=20210604153809, **n.d.**
34. T. Schuler, A. Chowdhury, A. T. Freiberg, B. Sneed, F. B. Spingler, M. C. Tucker, K. L. More, C. J. Radke, A. Z. Weber, *J. Electrochem. Soc.* **2019**, *166*, F3020. https://doi.org/10.1149/2.0031907jes.
35. M. R. Lee, H. Y. Lee, S. D. Yim, C. S. Kim, Y. G. Shul, A. Kucernak, D. Shin, *Fuel Cells* **2018**, *18*, 129. https://doi.org/10.1002/fuce.201700178.
36. H. A. Miller, K. Bouzek, J. Hnat, S. Loos, C. I. Bernäcker, T. Weißgärber, L. Röntzsch, J. Meier-Haack, *Sustain. Energy Fuels* **2020**, *4*, 2114. https://doi.org/10.1039/c9se01240k.
37. I. Vincent, E. C. Lee, H. M. Kim, *Sci. Rep.* **2021**, *11*. https://doi.org/10.1038/s41598-020-80683-6.
38. S. Seetharaman, R. Balaji, K. Ramya, K. S. Dhathathreyan, M. Velan, *Int. J. Hydrogen Energy* **2013**, *38*, 14934. https://doi.org/10.1016/j.ijhydene.2013.09.033.
39. X. Wu, K. Scott, *J. Mater. Chem.* **2011**, *21*, 12344. https://doi.org/10.1039/c1jm11312g.
40. M. Moura de Salles Pupo, R. Kortlever, *ChemPhysChem* **2019**, *20*, 2926. https://doi.org/10.1002/cphc.201900680.

13 of 13   **Electrochemical Science Advances**

RESEARCH ARTICLE
doi.org/10.1002/elsa.202100186

Chemistry
Europe
European Chemical
Societies Publishing

41. M. König, J. Vaes, E. Klemm, D. Pant, *iScience* **2019**, *19*, 135. https://doi.org/10.1016/j.isci.2019.07.014.

42. C. M. Gabardo, P. Colin, O. Brien, P. Jonathan, J. Li, H. Edward, D. Sinton, C. M. Gabardo, C. P. O. Brien, J. P. Edwards, C. Mccallum, Y. Xu, C. Dinh, J. Li, E. H. Sargent, D. Sinton, **2019**, 2777.

43. J. Liu, Z. Kang, D. Li, M. Pak, S. M. Alia, C. Fujimoto, G. Bender, Y. S. Kim, A. Z. Weber, *J. Electrochem. Soc.* **2021**, *168*, 054522.

44. S. Ringe, E. L. Clark, J. Resasco, A. Walton, B. Seger, A. T. Bell, K. Chan, *Energy Environ. Sci.* **2019**, *12*, 3001. https://doi.org/10.1039/C9EE01341E.

45. J. Resasco, Y. Lum, E. Clark, J. Z. Zeledon, A. T. Bell, *ChemElectroChem* **2018**, *5*, 1064. https://doi.org/10.1002/celc.201701316.

46. H. Hashiba, L. C. Weng, Y. Chen, H. K. Sato, S. Yotsuhashi, C. Xiang, A. Z. Weber, *J. Phys. Chem. C* **2018**, *122*, 3719. https://doi.org/10.1021/acs.jpcc.7b11316.

47. E. L. Clark, J. Resasco, A. Landers, J. Lin, L. T. Chung, A. Walton, C. Hahn, T. F. Jaramillo, A. T. Bell, *ACS Catal.* **2018**, *8*, 6560. https://doi.org/10.1021/acscatal.8b01340.

48. J. Resasco, A. T. Bell, *TrendsChem.* **2020**, *2*, 825. https://doi.org/10.1016/j.trechm.2020.06.007.

49. C. T. Dinh, T. Burdyny, G. Kibria, A. Seifitokaldani, C. M. Gabardo, F. Pelayo García De Arquer, A. Kiani, J. P. Edwards, P. De Luna, O. S. Bushuyev, C. Zou, R. Quintero-Bermudez, Y. Pang, D. Sinton, E. H. Sargent, *Science (80-.)*. **2018**, *360*, 783.

50. Y. C. Tan, K. B. Lee, H. Song, J. Oh, *Joule* **2020**, *4*, 1104.

SUPPORTING INFORMATION

Additional supporting information may be found in the online version of the article at the publisher's website.